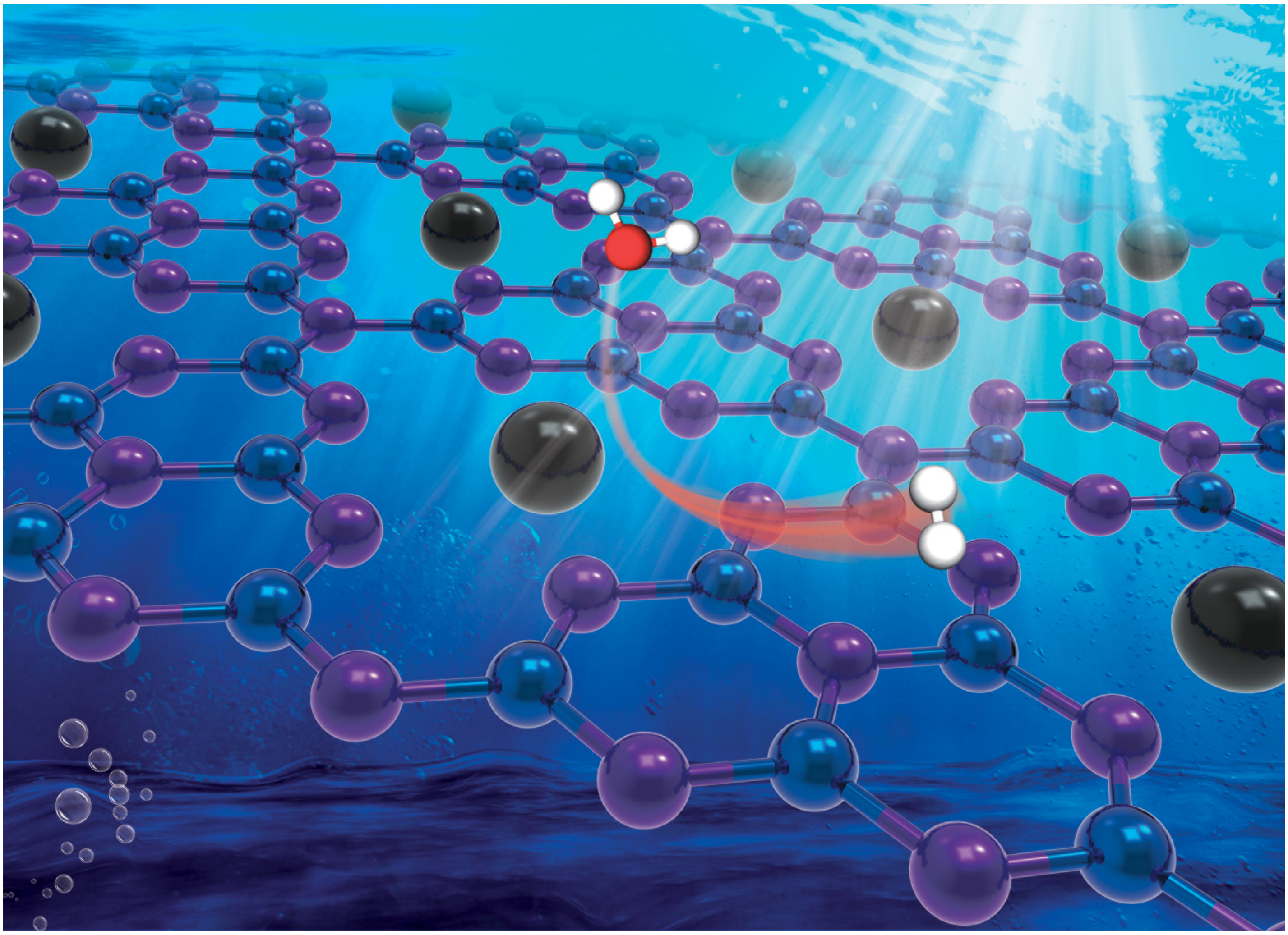

Showcasing research from the group of Professor Jie Ma and Dr Yongming Fu at Shanxi University, China.

Accelerating photocatalytic hydrogen production by anchoring Pt single atoms on few-layer g-C_3N_4 nanosheets with Pt–N coordination

Few-layer g-C_3N_4 nanosheets were successfully modified with Pt single atoms with 1.5 at% through low-temperature incipient wetness impregnation method, increasing the photocatalytic H_2 production rate by two orders of magnitude. Robust Pt–N_6 coordination was achieved by incorporating a Pt atom in the center of the sixfold cavity in g-C_3N_4.

As featured in:

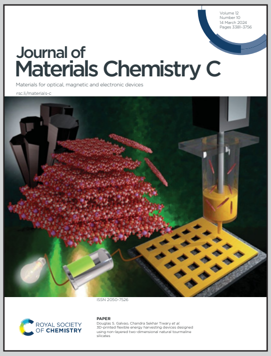

Volume 12
Number 10
14 March 2024
Pages 3381–3756

Journal of
Materials Chemistry C

Materials for optical, magnetic and electronic devices

rsc.li/materials-c

ISSN 2050-7526

ROYAL SOCIETY
OF CHEMISTRY

PAPER
Douglas S. Galvao, Chandra Sekhar Tiwary *et al.*
3D-printed flexible energy harvesting devices designed using non-layered two-dimensional natural tourmaline silicates

See Yongming Fu, Jie Ma *et al.*,
J. Mater. Chem. C, 2024, **12**, 3437.

ROYAL SOCIETY
OF **CHEMISTRY**

rsc.li/materials-c

Journal of
Materials Chemistry C

ROYAL SOCIETY
OF CHEMISTRY

PAPER

View Article Online
View Journal | View Issue

Check for updates

Cite this: *J. Mater. Chem. C*, 2024, **12**, 3437

Accelerating photocatalytic hydrogen production by anchoring Pt single atoms on few-layer g-C_3N_4 nanosheets with Pt–N coordination

Qi Zhang,[ab] Miao Yue,[ab] Peng Chen,[ab] Qingmiao Ren,[ab] Weihu Kong,[a] Chenxia Jia,[a] Qianyu Lu,[ab] Jizhou Wu,[abc] Yuqing Li,[abc] Wenliang Liu,[abc] Peng Li,[a] Yongming Fu*[ab] and Jie Ma*[abc]

Received 18th December 2023,
Accepted 4th February 2024

DOI: 10.1039/d3tc04673g

rsc.li/materials-c

Graphitic carbon nitride (g-C_3N_4) has gained considerable attention as a promising photocatalyst for hydrogen production through water splitting. However, its catalytic efficiency remains severely limited due to the rapid recombination of charge carriers and poor charge-transfer properties. Here, g-C_3N_4 is subjected to modification through the introduction of well-isolated Pt single atoms using a low-temperature incipient wetness impregnation method. The Pt single atoms exhibit a maximum weight ratio of 1.26%, resulting in a giant enhancement of the photocatalytic H_2 evolution rate (336.8 μmol h^{-1}), approximately two orders of magnitude higher than that of pristine g-C_3N_4 (1.8 μmol h^{-1}) during a 22-h-long test with an apparent quantum yield (AQY) of 13.5% at 405 nm. The improved performance and excellent stability in photocatalytic H_2 evolution can be attributed to the formation of Pt–N bonds between Pt single atoms and g-C_3N_4, which creates a new energy level of the N 2p–Pt 5d hybrid orbital for remarkably inhibiting the recombination of photogenerated electron–hole pairs and reducing interfacial charge-transfer resistance.

1. Introduction

Photocatalytic water splitting is anticipated to be an eco-friendly and enduring method for generating hydrogen (H_2) devoid of detrimental byproducts or emissions.[1–3] Extensive research has been conducted to identify the most suitable semiconductor-based photocatalysts that possess visible-light responsivity, stability, and reusability. In particular, carbon nitride allotropes have received extensive attention in photocatalysis due to their extended conjugation for fast separation and transfer of the charges.[4–6] Some studies indicate that graphitic carbon nitride (g-C_3N_4) has emerged as a highly promising candidate for photocatalytic water splitting due to its distinctive electronic structure, exceptional photoelectric characteristics, remarkable stability, and cost-effectiveness.[7–11] However, the efficiency of g-C_3N_4 in H_2 production is hindered by the limited carrier mobility and the rapid recombination of electron–hole pairs generated during the photocatalytic process.[12–14] To enhance the efficiency of photocatalytic H_2 production, a significant approach is the incorporation of cocatalysts, which can facilitate charge transfer and provide reactive sites.

Platinum (Pt) has been widely acknowledged as one of the most efficient cocatalysts for photocatalytic H_2 production due to its low overpotential and favorable Gibbs free energy in H_2 adsorption.[15–17] Traditional large-scale particulate Pt cocatalysts exhibit limited low atomic utilization and a scarcity of active sites, significantly constraining the utilization efficiency of Pt atoms. Consequently, it becomes imperative to incorporate Pt species in the form of clusters or even isolated single atoms, as this approach offers a viable strategy to optimize atomic efficiency.[18] With the reduction in the volume of the particulate cocatalyst, there is a progressive enhancement in both the specific surface area and atomic utilization. When the volume is decreased to atomic clusters comprising merely a few dozen atoms, a pronounced interaction between the support and the Pt atoms emerges, exerting a substantial effect on the photocatalytic process.[19–21] Ultimately, upon reducing the cocatalysts to a state of single atom dispersion, the ideal atom utilization attains 100% and the selectivity achieves its utmost level.[22–25] The presence of homogenous pores in layer-structured g-C_3N_4 offers stable coordination sites for anchor

---

[a] *School of Physics and Electronic Engineering & Institute of Laser Spectroscopy, State Key Laboratory of Quantum Optics and Quantum Optics Devices, Shanxi University, Taiyuan 030006, China. E-mail: fuyongming@sxu.edu.cn, mj@sxu.edu.cn*

[b] *Xinzhou Institute of Innovation Ecosystem, Shanxi University, Xinzhou 034000, China*

[c] *Collaborative Innovation Center of Extreme Optics, Shanxi University, Taiyuan 030006, China*

atoms, while the N atoms within the structure facilitate bonding between pyridine N and active atoms. Thus, g-C_3N_4 can serve as an appropriate support for the deposition of Pt single atoms, enabling efficient photocatalytic H_2 production.[26] In recent years, numerous investigations have documented diverse approaches for synthesizing single-atom Pt catalysts on g-C_3N_4, including ion exchange,[27] reflux reaction,[28] photoreduction,[29–33] and high-temperature pyrolysis.[34–38] Nevertheless, these methods face constraints when it comes to attaining high loading levels of single-atom Pt catalysts. In this respect, preparing Pt single atom anchored g-C_3N_4 with high loading and secure trapping is necessary to develop highly efficient photocatalysts.

In this study, the synthesis of Pt single atom anchored g-C_3N_4 nanosheets with varying Pt contents (Pt_x/g-C_3N_4) has been successfully achieved through a low-temperature incipient wetness impregnation method followed by high-temperature pyrolysis. The incipient wetness impregnation method is frequently employed to enhance the loading capacity of single atoms,[39–41] and lowering the impregnation temperature can additionally suppress the occurrence of agglomeration during the impregnation process. By employing the sequence of low-temperature incipient wetness impregnation, lyophilization, and high-temperature pyrolysis, the dispersion of high-density single atoms can be effectively improved. Characterization analyses have revealed that the isolated Pt single atoms are uniformly dispersed on the surface of g-C_3N_4, and the formation of Pt–N bonds notably enhances the charge separation and transfer capabilities. The photocatalytic rate of H_2 evolution for Pt_x/g-C_3N_4 demonstrates a notable increase compared to both pristine g-C_3N_4 and g-C_3N_4 modified with Pt nanoparticles.

2. Experimental

2.1. Synthesis of bulk g-C_3N_4 powder

Bulk g-C_3N_4 powder was synthesized through the thermal polymerization of urea. Specifically, 10 g of urea powder was placed in a closed alumina crucible within a muffle furnace (KSL-1100X-S, MTI, China) under a N_2 atmosphere. The furnace was gradually heated to 550 °C at a rate of 1 °C min^{-1} and maintained at this temperature for a duration of 2 h. Subsequently, the resulting yellow g-C_3N_4 powder was collected and allowed to cool to room temperature before further use.

2.2. Synthesis of few-layer g-C_3N_4 nanosheets

Few-layer g-C_3N_4 nanosheets were obtained through the process of ultrasonic-assisted liquid exfoliation. 100 mg of bulk g-C_3N_4 powder were dispersed in 100 mL of isopropanol and subjected to exfoliation using an ultrasonic crusher with a power of 1 kW for 12 h at room temperature. The resulting dispersion was then centrifuged using a high-speed centrifuge (HC-3018, Zonkia, China) at a speed of 8000 rpm for 10 min. The upper liquid was dried in a vacuum at 50 °C for 6 h to obtain pale yellow few-layer g-C_3N_4 nanosheets.

2.3. Synthesis of Pt_x/g-C_3N_4

The g-C_3N_4 nanosheets were loaded with Pt single atoms through low-temperature incipient wetness impregnation. A stable suspension was prepared by dispersing 100 mg of the as-prepared few-layer g-C_3N_4 nanosheets in 100 mL of deionized water and subjecting to ultrasonic treatment at a power of 200 W for 30 min. Subsequently, 0.5, 1, and 1.5 mL of H_2PtCl_6 solutions with a Pt concentration of 1 g L^{-1} were added drop by drop to the suspension. The resulting mixture was then transferred to a refrigerator and allowed to stand for 12 h at 0 °C to facilitate abundant adsorption, followed by rapid cooling to −60 °C. After undergoing freeze-drying in a freeze dryer (SCIENTZ-10N, Ningbo Scientz, China), the as-dried powders were transferred to a muffle furnace under a N_2 atmosphere and subjected to a heating process at 450 °C for 2 h to facilitate the generation of Pt single atoms on the surface of g-C_3N_4. Finally, the resulting products were dissolved in deionized water, filtered with a 0.22 μm PTFE filter membrane, and dried using a freeze dryer to remove any impurities. The as-prepared samples were designated as $Pt_{0.5}$/g-C_3N_4, Pt_1/g-C_3N_4, and $Pt_{1.5}$/g-C_3N_4, respectively. To establish a control, 10 mL of H_2PtCl_6 solution with a Pt concentration of 1 g L^{-1} was introduced into 100 mL of g-C_3N_4 solution and stirred for 30 min under xenon lamp irradiation to form Pt nanoparticles on few-layer g-C_3N_4.

2.4. Characterization

The Pt content of the samples was quantified using inductively coupled plasma-optical emission spectroscopy (ICP–OES, Agilent 5510, USA). The surface morphology was characterized with a scanning electron microscope (SEM, Regulus8230, Hitachi) and a transmission electron microscope (TEM, JEM-F200, JEOL) at an acceleration voltage of 200 kV. The identification of crystalline phases, chemical functional groups, and surface chemical states was performed using X-ray diffraction (XRD, Rigaku Miniflex 600, Japan), Fourier transform infrared spectroscopy (FTIR, Thermo Scientific Nicolet iS20, USA), and X-ray photoelectron spectrometry (XPS, Thermo Scientific K-Alpha, USA), respectively. The surface area analyzer (Quantachrome Nova 4000e, USA) was utilized to obtain the Brunauer–Emmett–Teller (BET) specific surface area and pore size distribution. Diffuse reflectance spectroscopy (DRS, Hitachi UH5700, Japan) was employed to acquire the UV-vis absorption spectroscopy data. High angle annular dark-field scanning transmission electron microscopy (HAADF–STEM) images were captured using an aberration corrected JEOL JEM-ARM200F operating at 200 keV. X-ray absorption spectroscopy (XAS) measurements of the Pt element were conducted at the XAS beam line of the Shanghai Synchrotron Radiation Facility (SSRF) utilizing an Si(111) double-crystal monochromator, where the experimental data were acquired in the fluorescence mode using an ionization chamber. The steady and time-resolved photoluminescence (PL) spectra were measured using a photoluminescence spectrometer (Edinburgh FLS1000, UK).

2.5. Photoelectrochemical measurements

Electrochemical measurements were performed using an electrochemical workstation (CHI 660E, China) with a standard three-electrode system. The Ag/AgCl electrode and Pt foil were used as the reference electrode and counter electrode in 0.5 M Na_2SO_4 aqueous solution, respectively. Fluorine–tin oxide (FTO) glass coated with the photocatalyst was used as the working electrode. To prepare the working electrode, 5 mg of the photocatalyst was dispersed in 1 mL of ethanol and 20 μL of Nafion anisole solution (5%) under ultrasonic treatment for 30 min to form a homogeneous slurry. Then, 50 μL of the obtained slurry was dropped on the conductive surface (10 mm × 10 mm) of FTO (10 mm × 30 mm × 1.1 mm) using a pipette and dried at 60 °C for 2 h. The transient photocurrent curves were measured in the *i*–*t* mode by periodically switching a 300 W Xe-lamp (PLS-SXE300, Perfectlight, China) at a 20 s interval under a continuous bias of 0.2 V. The electrochemical impedance spectroscopy (EIS) was conducted at an open circuit voltage with frequency ranging from 0.01 to 100 kHz and an amplitude of 5 mV.

2.6. Photocatalytic H_2 evolution

Photocatalytic water splitting reactions were implemented in a photocatalytic trace-gas generation and analysis system (Labsolar-6A, Perfectlight, China), involving a sealed top-irradiation quartz vessel connected to a closed gas circulation system. In a typical experiment, 50 mg of photocatalysts were added to 90 mL of deionized water and 10 mL of triethanolamine (TEOA) was added as a sacrificial agent. Prior to the photocatalytic test, the air in the reactor is evacuated using a vacuum pump. The evolved H_2 gas was analyzed every 30 min using gas chromatography (GC-2060, FULI, China) with N_2 serving as carrier gas. During the photocatalytic test, a simulated sunlight source was provided by the 300 W Xe-lamp. The reaction temperature was maintained at 2 °C using a cooling water circulator. The apparent quantum yield (AQY) of $Pt_{1.5}/g\text{-}C_3N_4$ was determined using the same equipment under irradiation passing through different bandpass filters (365, 405, 420 and 500 nm, respectively) for 4 h. The AQY value was calculated using eqn (1),

$$\begin{aligned}\mathrm{AQY} &= \frac{2 \times \text{number of evolved hydrogen}}{\text{number of incident photons}} \times 100\% \\ &= \frac{2RN_{\mathrm{A}}hc}{IA\lambda} \times 100\%\end{aligned} \tag{1}$$

where R represents the H_2 evolution rate, N_A is the Avogadro constant, h is the Planck constant, c is the speed of light, I is the light intensity, A is the irradiation area, and λ is the illumination wavelength.

3. Results and discussion

$g\text{-}C_3N_4$ samples loaded with varying Pt contents have been successfully synthesized using the low-temperature incipient wetness impregnation method, and the ICP–OES analysis reveals that the actual Pt loading percentages of $Pt_{0.5}/g\text{-}C_3N_4$, $Pt_1/g\text{-}C_3N_4$, $Pt_{1.5}/g\text{-}C_3N_4$ and $Pt_{NP}/g\text{-}C_3N_4$ are determined to be 0.38%, 0.90%, 1.26%, and 3.95%, respectively. The observed loss in Pt content can potentially be attributed to incomplete adsorption of Pt species on the surface of $g\text{-}C_3N_4$ during low-temperature treatment. The XRD patterns of all the samples exhibit two characteristic diffraction peaks at 12.9° and 27.7° (Fig. 1a), which correspond to the (100) and (002) planes of hexagonal $g\text{-}C_3N_4$. No discernible peaks or peak-shifts associated with Pt species can be observed for the $Pt_x/g\text{-}C_3N_4$ samples, suggesting that the presence of Pt does not significantly alter the crystal structure of $g\text{-}C_3N_4$. The FTIR spectrum of few-layer $g\text{-}C_3N_4$ demonstrates distinct peaks at approximately 3100–3500, 1200–1600, and 810 cm^{-1}, which correspond to the vibrational modes of N–H/O–H bonds, aromatic C–N heterocyclic units, and triazine units, respectively (Fig. 1b).[34] The FTIR spectra of the $Pt_x/g\text{-}C_3N_4$ samples exhibit similar peaks to that of pristine $g\text{-}C_3N_4$, suggesting that the introduction of Pt species does not alter the chemical composition of $g\text{-}C_3N_4$.

The BET analyses are depicted in Fig. 2. The N_2 adsorption–desorption isotherms of the samples exhibit a type-IV behavior (Fig. 2a), indicating the presence of mesopores. The BET surface areas of $g\text{-}C_3N_4$ and $Pt_{0.5}/g\text{-}C_3N_4$ are 71.097 and 132.904 $m^2\ g^{-1}$,

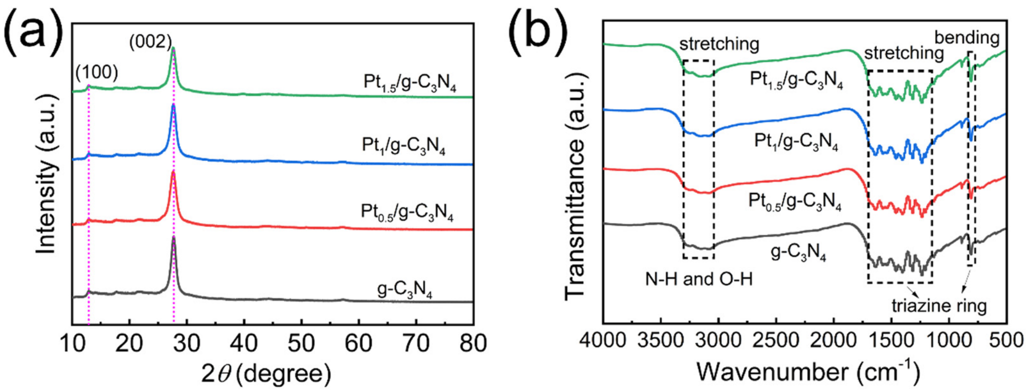

Fig. 1 (a) XRD patterns. (b) FTIR spectra.

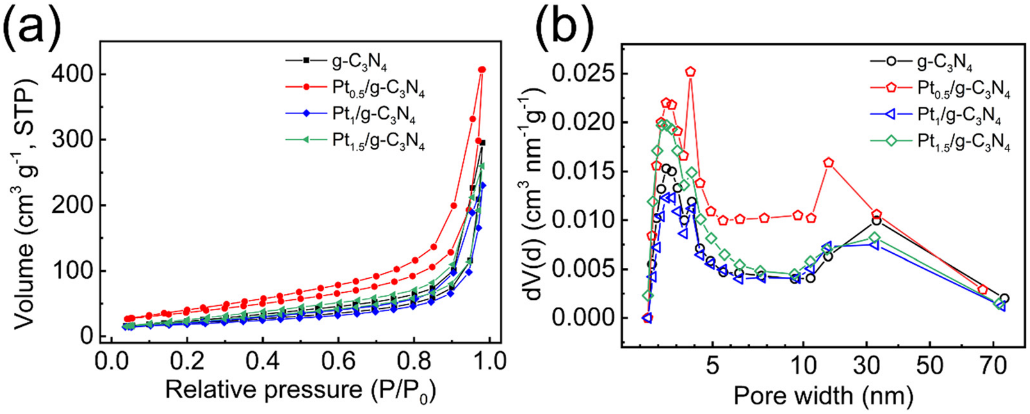

Fig. 2 (a) N_2 adsorption–desorption isotherm. (b) Pore size distributions.

respectively. Fig. 2b displays a quite wide distribution of pore size, confirming the existence of both micropores and mesopores. Interestingly, the pore volumes of pristine $g\text{-}C_3N_4$, $Pt_{0.5}/g\text{-}C_3N_4$, $Pt_1/g\text{-}C_3N_4$, and $Pt_{1.5}/g\text{-}C_3N_4$ are 0.322, 0.539, 0.268, and 0.302 $cm^3\ g^{-1}$, while the mean pore diameters of these samples are 2.571, 1.897, 2.197, and 1.963 nm, respectively, implying that the adsorption behavior is primarily influenced by micropores and the presence of Pt atoms can enhance the formation of micropores to provide more active sites. The significant increase in the surface area and pore volume of $Pt_{0.5}/g\text{-}C_3N_4$ can be attributed to the fact that the uniform dispersion of isolated Pt atoms can enlarge the interlayer distance of $g\text{-}C_3N_4$ structures.[27,42,43] As the Pt content exceeds 0.5%, the specific surface area and pore volume exhibit a declining trend, but $Pt_x/g\text{-}C_3N_4$ still demonstrates the ability to offer an increased number of micropores as active sites for the photocatalytic reaction.

Fig. 3 presents the XPS analysis conducted on the samples to examine their chemical composition and oxidation states. The survey spectra indicate the presence of C and N in the $g\text{-}C_3N_4$ sample and Pt in the $Pt_x/g\text{-}C_3N_4$ and $Pt_{NP}/g\text{-}C_3N_4$ samples

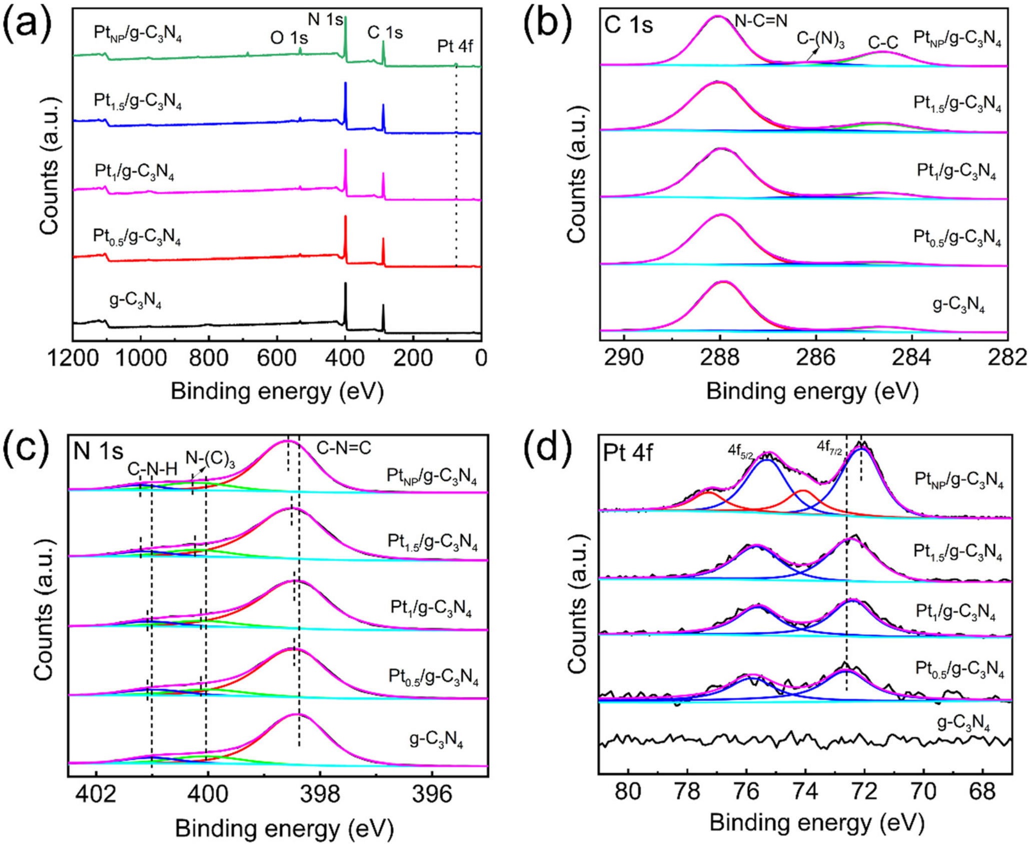

Fig. 3 XPS spectra of the samples. (a) Survey. (b) C 1s. (c) N 1s. (d) Pt 4f.

(Fig. 3a). The high-resolution C 1s spectra are well fitted to three distinct peaks at 287.98, 286.02, and 284.6 eV, corresponding to the N–C═N, C–(N)$_3$, and C═C bonds, respectively (Fig. 3b).[44] In the N 1s spectrum of g-C_3N_4, there are three characteristic peaks including 398.36 eV for C–N═C, 400.04 eV for N–(C)$_3$, and 401.00 eV for C–N–H, respectively (Fig. 3c).[44] Compared to g-C_3N_4, the three peaks of N 1s shift towards higher energy with increasing Pt loading.[40] For $Pt_{1.5}$/g-C_3N_4, the shift values assigned to C–N═C, N–(C)$_3$, and C–N–H groups are 0.09, 0.14, and 0.13 eV, respectively. The binding energy of N 1s in Pt_{NP}/g-C_3N_4 exhibits a similar shift.[45] In Fig. 3d, the Pt 4f spectrum of Pt_{NP}/g-C_3N_4 is divided into two sets of double peaks, with the high-energy and low-energy peaks corresponding to the high-oxidation state of Pt clusters and metallic Pt nanoparticles, respectively.[28,46,47] The Pt $4f_{7/2}$ and $4f_{5/2}$ orbitals related to Pt nanoparticles are located at 72.05 and 75.25 eV, while those of Pt_x/g-C_3N_4 are located at 72.45 and 75.65 eV, respectively.[46,48] The Pt 4f orbitals of Pt_x/g-C_3N_4 roughly corresponding to Pt^{2+} species positively shift by 0.4 eV compared to Pt nanoparticles, which is ascribed to the weakened shielding effect due to the lack of 5d electrons of the outer orbital.[47,49] Therefore, the alteration in the electron density of the N atom is ascribed to the modification of the Pt atom, thereby confirming the robust electronic interaction between Pt and N atoms (Pt–N bond) at higher density of Pt single atoms.

The distribution and configuration of Pt atoms at high loading density in $Pt_{1.5}$/g-C_3N_4 are accurately determined through the characterization of an HAADF–STEM image, as illustrated in Fig. 4. Fig. 4a and b are the SEM images of $Pt_{1.5}$/g-C_3N_4 and Pt_{NP}/g-C_3N_4, indicating that the nanosheets remain ultra-thin after the introduction of Pt species. The corresponding

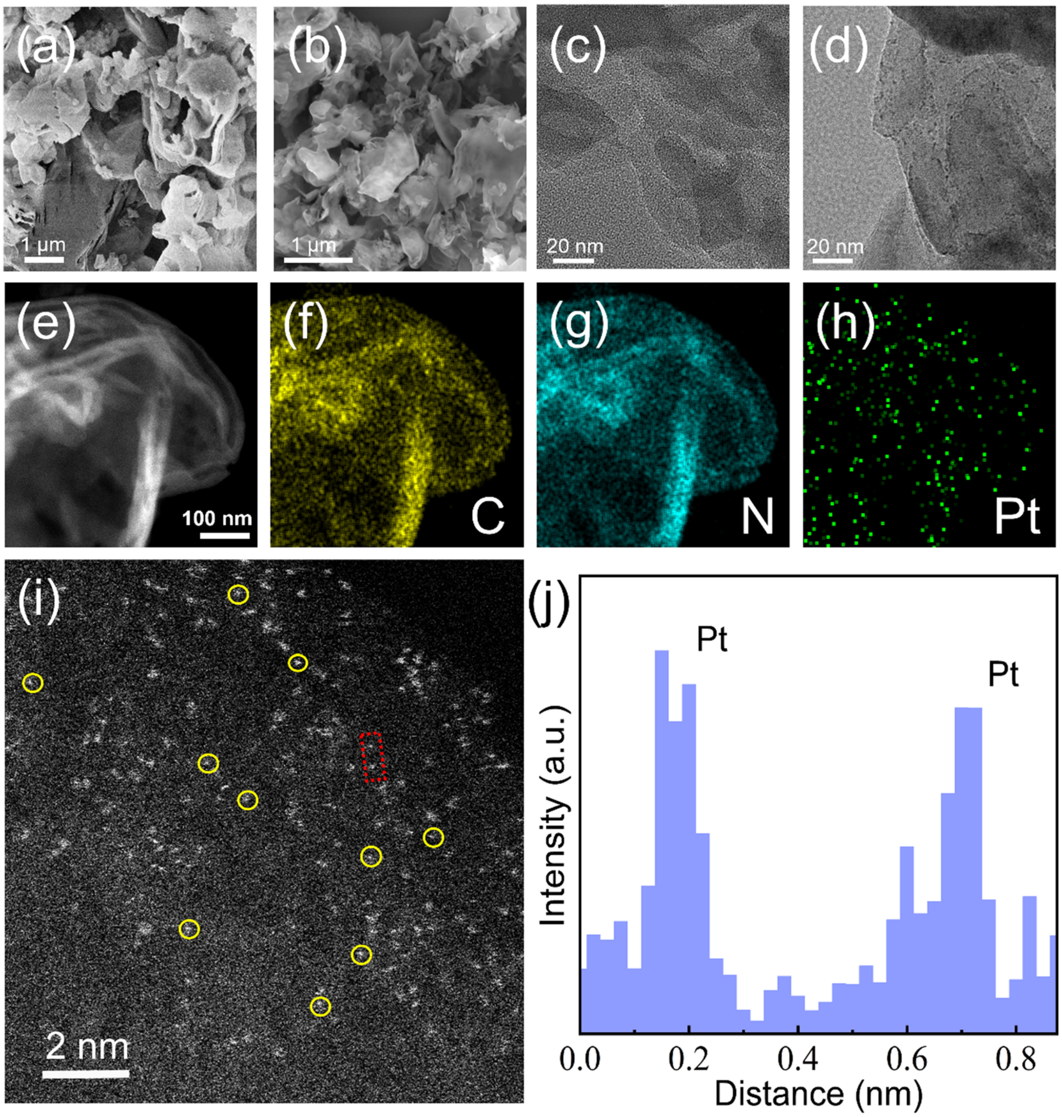

Fig. 4 Morphology of $Pt_{1.5}$/g-C_3N_4 and PtNP/g-C_3N_4. (a) and (b) SEM images of $Pt_{1.5}$/g-C_3N_4 and PtNP/g-C_3N_4. (c) and (d) TEM images of $Pt_{1.5}$/g-C_3N_4 and PtNP/g-C_3N_4. (e) Low-resolution STEM image. (f)–(h) Elemental mapping of C, N, and Pt. (i) HAADF-STEM image. (j) Intensity profile of two Pt single atoms along the middle of the red rectangle in (i).

high-resolution TEM images are shown in Fig. 4c and d, respectively. The Pt nanoparticles can only be observed in $Pt_{NP}/g\text{-}C_3N_4$. Fig. 4e provides a low-resolution STEM depiction of the crumpled few-layer structure of $Pt_{1.5}/g\text{-}C_3N_4$. The elemental mapping profiles presented in Fig. 4f–h demonstrate the homogeneous distribution of C, N, and Pt elements, confirming the presence of trace Pt atoms dispersed throughout $g\text{-}C_3N_4$. Furthermore, the HAADF–STEM image in Fig. 4i reveals densely dispersed bright spots corresponding to Pt atoms, which exist in an isolated single-atom state on the surface of $g\text{-}C_3N_4$. To quantify the dispersion of Pt single atoms, the distance between adjacent Pt single atoms is determined to be approximately 0.5 nm (Fig. 4j), suggesting a high level of dispersion and individualization of Pt atoms.

The detailed atomic-level structure and coordination information on Pt species is provided by synchrotron-based X-ray absorption near-edge structure (XANES) and extended X-ray absorption fine structure (EXAFS) at the Pt L_3-edge. $Pt_1/g\text{-}C_3N_4$ and $Pt_{1.5}/g\text{-}C_3N_4$ exhibit identical XANES spectra with the absorption edge intensity falling between that of Pt foil and PtO_2 (Fig. 5a), confirming that the Pt single atoms in $Pt_x/g\text{-}C_3N_4$ are highly reduced to an oxidation state between Pt^0 and Pt^{4+}.[50] The correlation between the peak intensity of L_3-edge absorption and the unoccupied density of states of Pt 5d orbitals is evident.[51] Thus, the Pt atoms in $Pt_x/g\text{-}C_3N_4$ possess a greater abundance of unoccupied 5d-electron states, which aligns with the observed electron transfer indicated by the Pt 4f XPS spectra. To further analyze the local coordination environment of the Pt single atoms, Fourier-transform EXAFS analysis is performed (Fig. 5b). The peaks observed in the spectra correspond to distinct coordination shells surrounding the Pt atoms. The prominent peaks of Pt foil and PtO_2 are clearly observed at 2.55 and 1.60 Å, respectively. However, these peaks are absent for $Pt_1/g\text{-}C_3N_4$ and $Pt_{1.5}/g\text{-}C_3N_4$, confirming the presence of Pt single atoms, which is consistent with the HAADF–STEM observation. Previous studies have shown that Pt single atoms can be stabilized through covalent bonds with adjacent N and C atoms.[27,47,50,52] Therefore, the dominant peak at approximately 1.9 Å can be assigned to the Pt–N/C bonds. In this case, the experimental EXAFS spectra of $Pt_1/g\text{-}C_3N_4$ and $Pt_{1.5}/g\text{-}C_3N_4$ exhibit a satisfactory fit while employing the Pt–N/C pathway. Although the exact coordination of Pt atoms with either N or C presents difficulties, it is more probable to observe Pt–N coordination by examining the significant energy shift of N 1s spectra of $Pt_x/g\text{-}C_3N_4$. Based on the EXAFS fitting outcomes (Fig. 5c and d), both the $Pt_1/g\text{-}C_3N_4$ and $Pt_{1.5}/g\text{-}C_3N_4$ demonstrate comparable coordination numbers (Pt_1–N: 6.3 ± 0.4; $Pt_{1.5}$–N: 6.4 ± 0.4) and Pt–N bond lengths (∼2.41 Å). It should also be noted that when the Pt atom is situated within the central position of a sixfold cavity in $g\text{-}C_3N_4$, it is expected to exhibit a Pt–N bond length of approximately 2.38 Å.[40] The EXAFS wavelet transforms provide a method to obtain both the radial distance resolution (*R* space) and *k* space resolution simultaneously. Fig. 6a and b show that the maximum intensities of $Pt_1/g\text{-}C_3N_4$ and $Pt_{1.5}/g\text{-}C_3N_4$ centered at about 6.55 and 6.30 $Å^{-1}$ (*k* space) are resolved at 1.90 Å (*R* space), respectively,

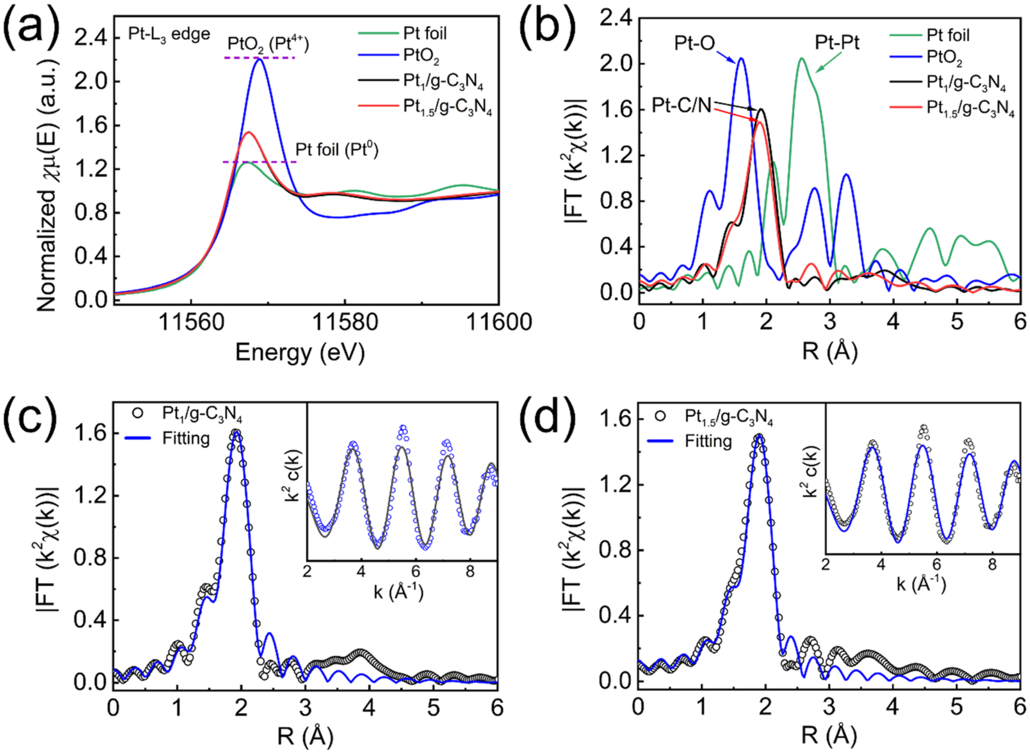

Fig. 5 XAFS of $Pt_1/g\text{-}C_3N_4$ and $Pt_{1.5}/g\text{-}C_3N_4$. (a) L_3-edge XANES spectra. (b) k^2-weighted FT-EXAFS spectra. (c) Fitted FT-EXAFS spectra of $Pt_1/g\text{-}C_3N_4$. (d) Fitted FT-EXAFS spectra of $Pt_{1.5}/g\text{-}C_3N_4$.

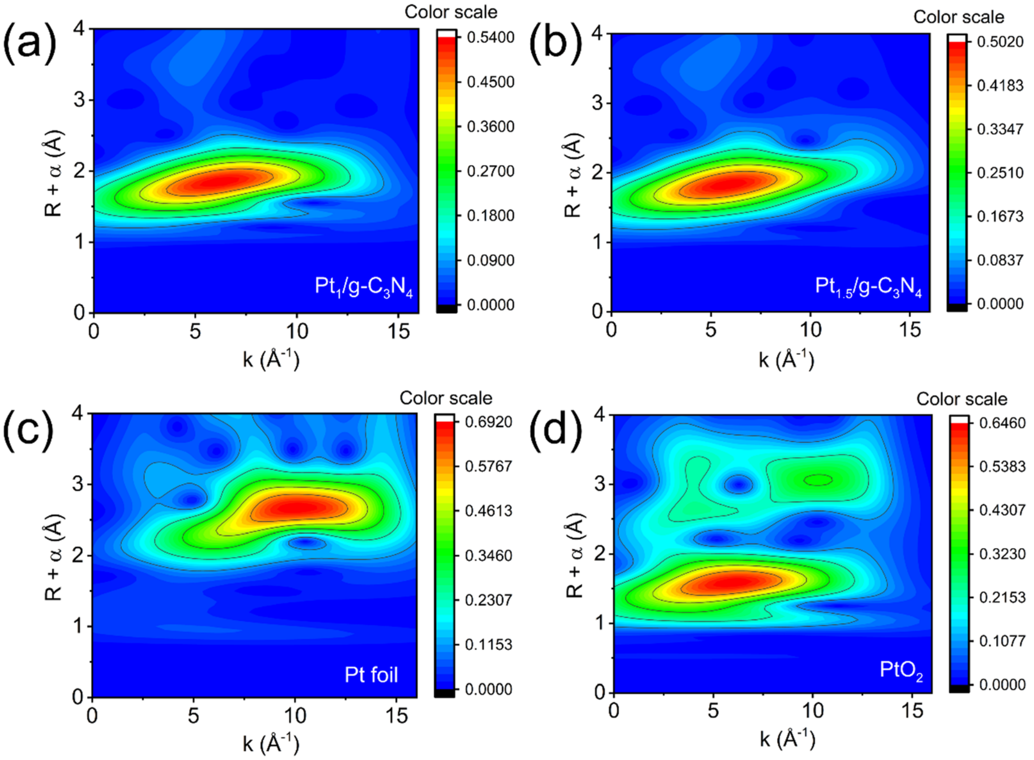

Fig. 6 WT-EXAFS of (a) Pt foil, (b) PtO$_2$, (c) Pt$_1$/g-C$_3$N$_4$, and (d) Pt$_{1.5}$/g-C$_3$N$_4$.

which are both assigned to the Pt–N coordination structure.[45,53] Note that the intensities corresponding to Pt–Pt (10.05 Å^{-1}, Fig. 6c) and Pt–O (6.05 Å^{-1}, Fig. 6d) coordination for the Pt foil and PtO$_2$ are not observed for Pt$_1$/g-C$_3$N$_4$ and Pt$_{1.5}$/g-C$_3$N$_4$. The coordination analyses provide confirmation of the highly reduced state of the Pt single atoms and their strong interaction with N atoms in an isolated state.

The band structures of the samples are depicted in Fig. 7. The DRS results indicate an increasing absorption intensity in the UV region and a slight red-shift in the absorption edge at approximately 430 nm with increasing Pt content (Fig. 7a), which can be ascribed to the presence of a higher concentration of Pt–N bonds.[34] By extrapolating the intercept of the *x*-axis in the linear region of Tauc plots, the band gaps (E_g) of g-C$_3$N$_4$ and Pt$_x$/g-C$_3$N$_4$ are calculated to be 2.67, 2.63, 2.60, and 2.59 eV, respectively (Fig. 7b).[54] The corresponding valence band potentials (E_{VB}) are calculated using valence band XPS (V$_B$-XPS), yielding values of 1.89, 1.75, 1.20, and 1.17 eV, respectively (Fig. 7c). The E_{VB} and the standard hydrogen electrode ($E_{VB,NHE}$) exhibit a correlation expressed as $E_{VB,NHE} = \varphi + E_{VB,XPS} - 4.44$, where φ represents the work function of the XPS analyzer (4.2 eV).[55] Thus, the $E_{VB,NHE}$ values of the respective samples are determined to be 1.65, 1.51, 1.02, and 0.93 eV. The band structures of g-C$_3$N$_4$ and Pt$_x$/g-C$_3$N$_4$ are shown in Fig. 7d, where the conduction band potential (E_{CB}) is calculated using the empirical formula: $E_{CB} = E_{VB} - E_g$. It is noteworthy that the E_{CB} of Pt$_x$/g-C$_3$N$_4$ tends to be more negative than that of g-C$_3$N$_4$, suggesting that Pt$_x$/g-C$_3$N$_4$ has a stronger reduction in protons compared to g-C$_3$N$_4$ in thermodynamics.

The PL spectra reveal that all of the samples show a similar intrinsic fluorescence emission peak within the range of 400–550 nm (Fig. 8a).[30] The PL intensity of Pt$_x$/g-C$_3$N$_4$ is significantly diminished as a result of the incorporation of Pt single atoms, indicating a pronounced suppression of recombination of photogenerated charge carriers.[22,46,56] The time-resolved PL-decay spectrum fitted by third-order exponential terms provides direct evidence of the duration of the photo-excited charge carriers (Fig. 8b), showing that the presence of Pt single atoms leads to a shorter lifetime (6.00, 5.80, and 5.90 ns for Pt$_{0.5}$/g-C$_3$N$_4$, Pt$_1$/g-C$_3$N$_4$, and Pt$_{1.5}$/g-C$_3$N$_4$, respectively) compared to g-C$_3$N$_4$ (8.09 ns). The rapid migration of charge carriers between Pt single atoms and g-C$_3$N$_4$ enhances exciton dissociation, thereby effectively inhibiting the recombination of electron–hole pairs.[49] To assess the charge-separation ability, the photocurrent and EIS properties are examined. In Fig. 8c, the photoelectrode of Pt$_x$/g-C$_3$N$_4$ shows a higher photocurrent density in comparison to g-C$_3$N$_4$, indicating superior charge-transfer properties and more efficient photogenerated charge separation in Pt$_x$/g-C$_3$N$_4$. Furthermore, the EIS Nyquist plot of Pt$_x$/g-C$_3$N$_4$ displays a smaller semicircle compared to g-C$_3$N$_4$ (Fig. 8d), suggesting enhanced charge-transfer ability at the photocatalyst interface and improved electronic utilization. These results indicate that the incorporation of well-dispersed Pt single atoms can effectively augment optical absorption, diminish the band gap and valence band, impede photogenerated carrier recombination, and facilitate interfacial charge transfer. Moreover, the improving effect becomes stronger with the increasing content of Pt single atoms. These outcomes hold

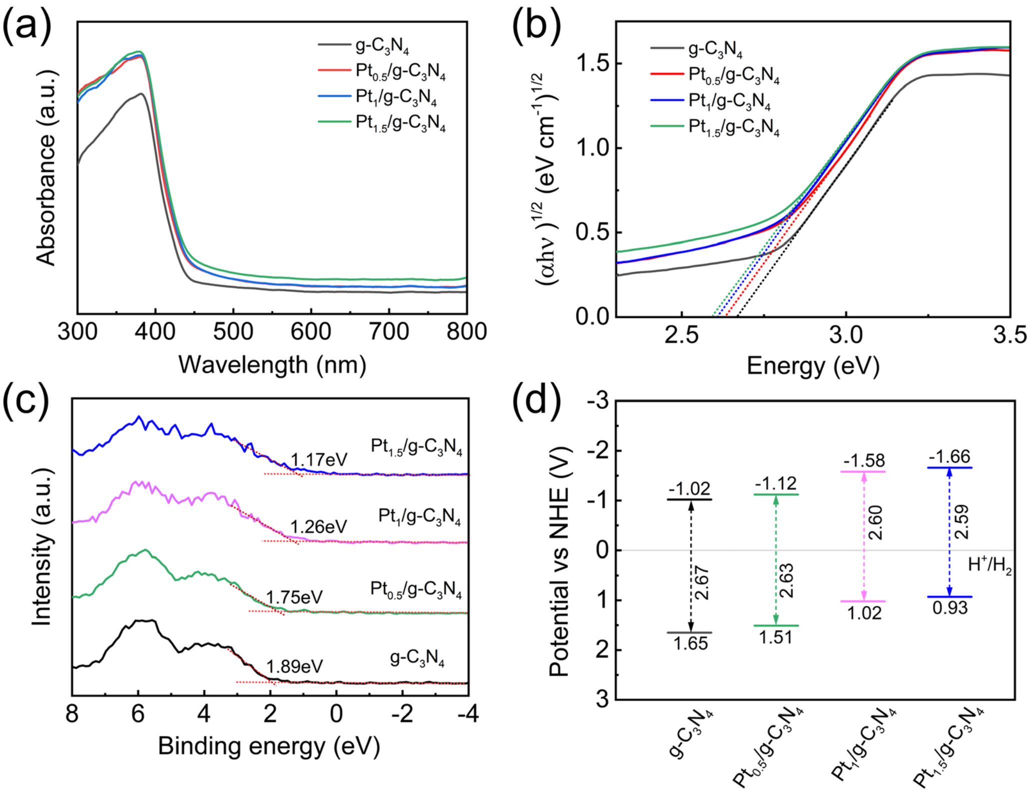

Fig. 7 (a) UV-vis DRS. (b) Tauc plots. (c) VB-XPS. (d) Schematic band structures.

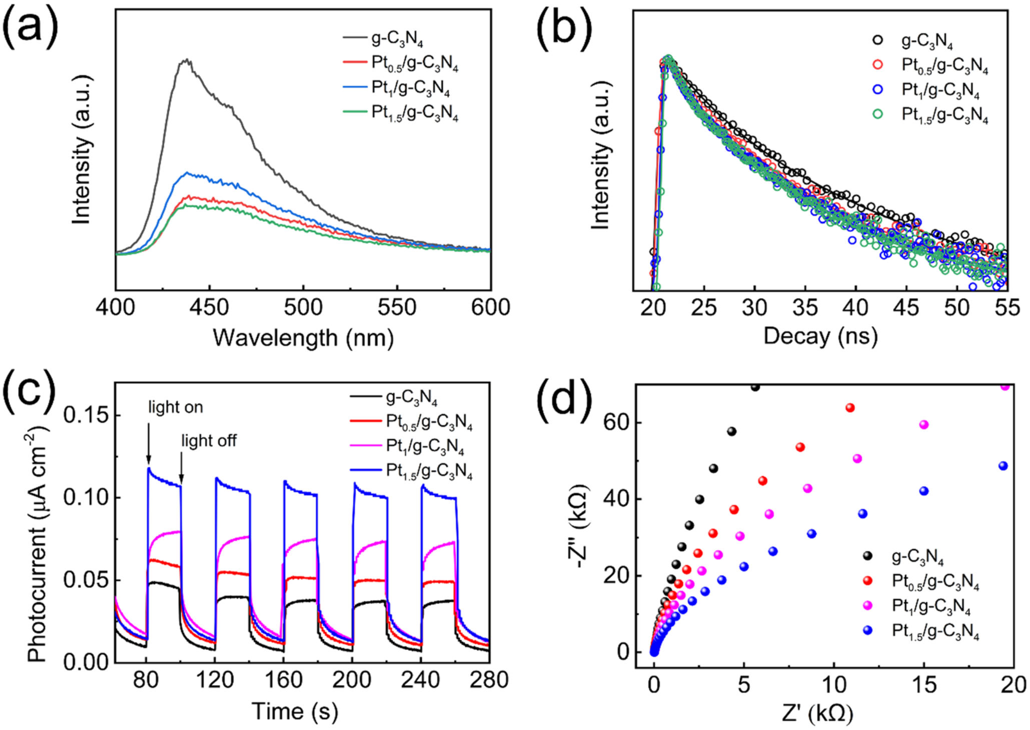

Fig. 8 (a) PL spectra. (b) Time-resolved PL spectra. (c) Transient photocurrent responses. (d) EIS Nyquist plots.

significant implications for enhancing the efficiency of the photocatalytic H_2 evolution reaction.

The advantage of loading Pt single atoms in photocatalytic H_2 evolution is evaluated by varying the Pt content and

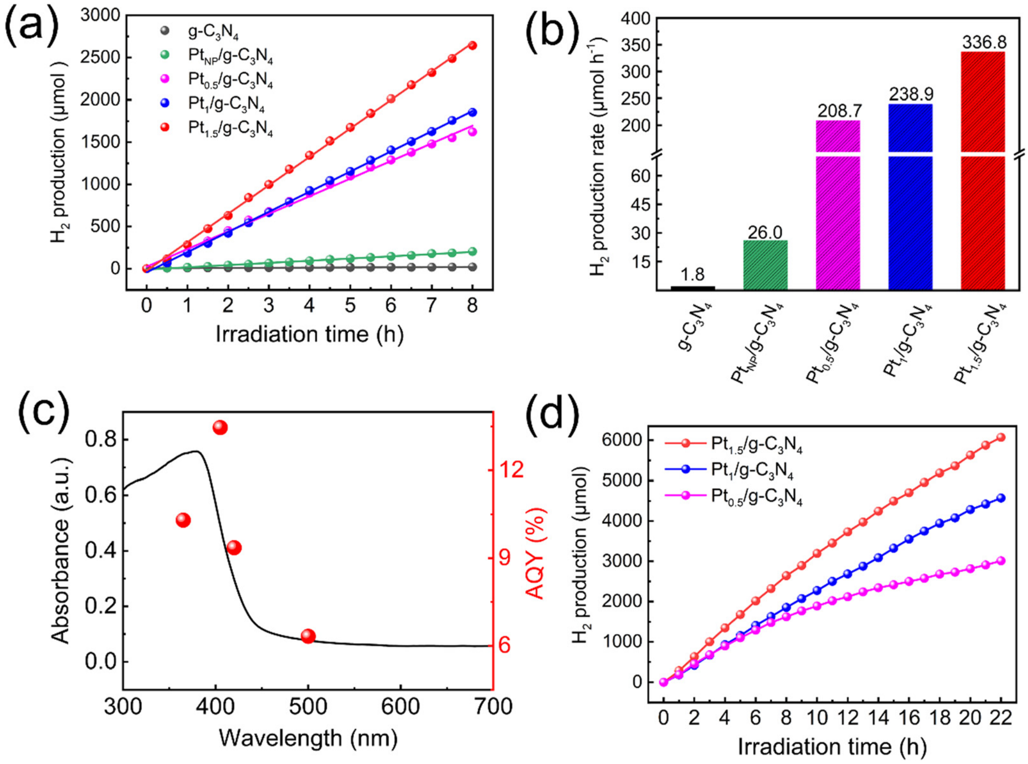

Fig. 9 (a) Time courses for photocatalytic H_2 evolution of Pt_x/g-C_3N_4 under Xe-lamp irradiation. (b) Corresponding photocatalytic H_2 evolution rate. (c) AQY of $Pt_{1.5}$/g-C_3N_4. (d) Stability tests for 22 h.

aggregation. As shown in Fig. 9a, the initial H_2 production rate of pristine g-C_3N_4 is relatively low (1.8 μmol h^{-1}), which experiences an increase to 26.0 μmol h^{-1} upon loading Pt nanoparticles. Once g-C_3N_4 is modified with Pt single atoms at a loading content of merely 0.5%, a substantial enhancement of the photocatalytic H_2 production rate is achieved (208.7 μmol h^{-1}). The H_2 production rate of $Pt_{0.5}$/g-C_3N_4 is ∼116 times that of g-C_3N_4 and ∼8 times that of Pt_{NP}/g-C_3N_4, despite the amount of Pt source being only 1/20th of Pt_{NP}/g-C_3N_4. With an increase in Pt concentration, Pt_1/g-C_3N_4 and $Pt_{1.5}$/g-C_3N_4 exhibit elevated H_2 production rates of 238.9 and 336.8 μmol h^{-1}, respectively (Fig. 9b). These results indicate a positive correlation between the H_2 production rate and the loading content of Pt single atoms within a reasonable range. The AQY of $Pt_{1.5}$/g-C_3N_4 under irradiation at different wavenumbers is shown in Fig. 9c. Against irradiation wavenumbers of 365, 405, 420, and 500 nm, the AQYs are 10.30%, 13.46%, 9.35%, and 6.32%, respectively. The high AQY value and the good match between AQY and the absorption spectrum indicate that most of the captured photons are involved in the photocatalytic reaction.[45,57] Compared with other Pt single-atom modified g-C_3N_4 photocatalysts prepared by different methods, $Pt_{1.5}$/g-C_3N_4 reported in this work exhibits a relatively high loading content of Pt single atoms and excellent photocatalytic H_2 evolution performances, as shown in Table 1.[28,40,49,58,59]

To study the stability of photocatalytic H_2 production, an extended duration of the H_2 evolution test is conducted. Fig. 9d shows that the H_2 production rate of $Pt_{0.5}$/g-C_3N_4 experiences a noticeable decline after 10 h, which may be attributed to the rupture of the Pt–N bond resulting from inadequate Pt filling between 3-*s*-triazines. Interestingly, the H_2 production rates of Pt_1/g-C_3N_4 and $Pt_{1.5}$/g-C_3N_4 remain relatively constant for 22 h, indicating that the sufficient dispersion of Pt single atoms facilitates an optimal and robust interaction with g-C_3N_4. To further investigate the reusability, the photocatalytic test of $Pt_{1.5}$/g-C_3N_4 is repeated four times, and the used catalyst after

Table 1 A comparison of the photocatalytic H_2 production efficiency of $Pt_{1.5}$/g-C_3N_4 reported in this work with those of other Pt single-atom modified g-C_3N_4 photocatalysts

Samples	Pt loading	Methods	Light sources	H_2 production rates (μmol h^{-1})	AQYs	Ref.
Pt–CN	0.74%	Immersion	30 W LED ($\lambda > 520$)	34.2	0.84% λ = 520 nm	28
Pt/CN	0.16%	Immersion	300 W Xe lamp ($\lambda > 420$)	318	—	40
Pt/CN	0.11%	Photo-chemical reduction	300 W Xe lamp (AM1.5)	40.1	—	49
Pt-CN	0.38%	Immersion	300 W Xe lamp (AM1.5)	2.9	—	58
Pt_{HD}-CNNT	0.32%	Pyrolysis	300 W Xe lamp ($\lambda > 420$)	106.1	13.1% λ = 420 nm	59
$Pt_{1.5}$/g-C_3N_4	1.26%	IWI	300 W Xe lamp	336.8	13.5% λ = 405 nm	This work

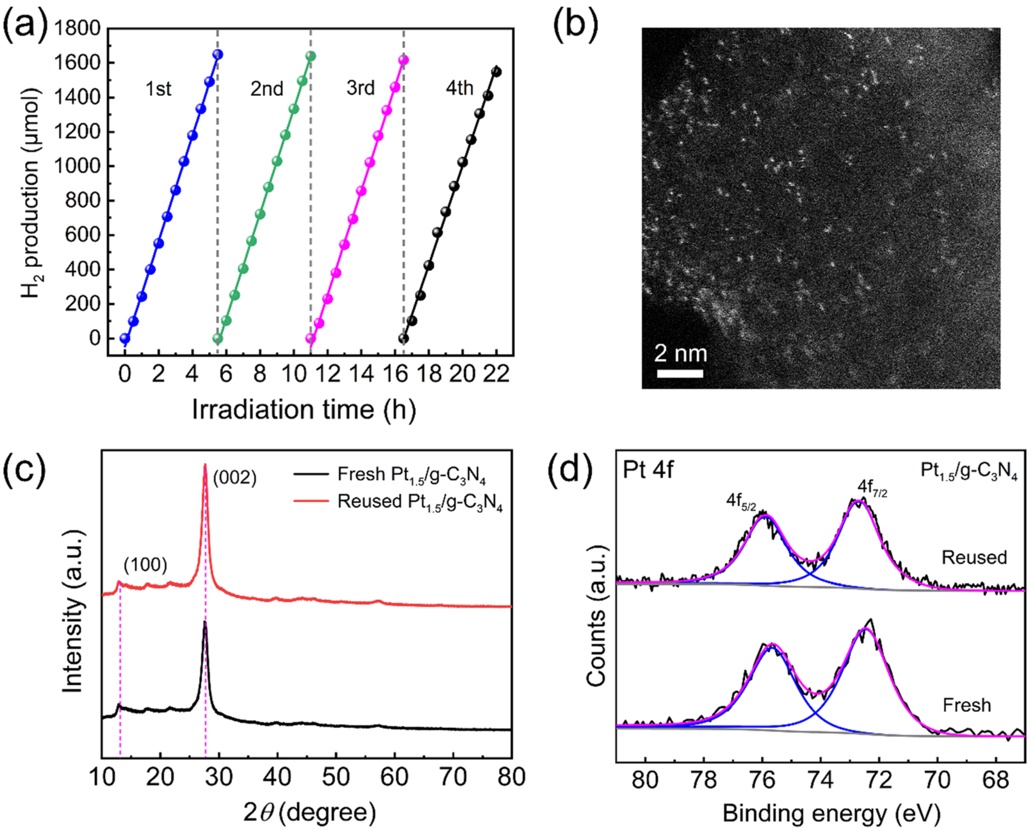

Fig. 10 Reusability of $Pt_{1.5}/g\text{-}C_3N_4$. (a) The photocatalytic H_2 production rate during four cycles. (b) HAADF-STEM image after reaction. (c) and (d) Comparison before and after photocatalytic reaction of (c) XRD and (d) XPS Pt 4f.

the reaction is characterized again, as depicted in Fig. 10. Fig. 10a shows the H_2 production rate of $Pt_{1.5}/g\text{-}C_3N_4$ during four cycles. After four cycles, the H_2 production capability is 5.8% lower than the initial value, exhibiting excellent photocatalytic stability. The HAADF–STEM image of $Pt_{1.5}/g\text{-}C_3N_4$ after photocatalysis is shown in Fig. 10b, indicating that the Pt single atoms maintain a high dispersion in an isolated state without apparent aggregation. Comparing the XRD patterns (Fig. 10c) and Pt 4f XPS spectra (Fig. 10d) before and after 4-cycle-photocatalysis, both the structure of $g\text{-}C_3N_4$ and the valence state of Pt single atoms are not significantly changed. These results demonstrate that $Pt_x/g\text{-}C_3N_4$ exhibits excellent photocatalytic stability after a long photocatalytic reaction even when loaded with a high density of Pt single atoms.

The enhanced mechanism of photocatalytic H_2 production of $Pt_x/g\text{-}C_3N_4$ is illustrated in Fig. 11. Low-temperature treatment reduces the average pore size of the small pores in $g\text{-}C_3N_4$, which may promote the adsorption of H^+. Furthermore, the strong interaction between Pt 5d and N 2p for the formation of the Pt–N bond plays a key role in the kinetics of the H_2 evolution reaction by effectively accelerating charge transfer and stabilizing active sites for photocatalysis.[34,40,42,60] Pt single atoms incorporated in the center of the sixfold cavity and forming robust $Pt\text{–}N_6$ coordination introduce new energy levels within the band structure of $g\text{-}C_3N_4$, leading to improved separation of photo-induced electron–hole pairs. Under light irradiation, the photogenerated electrons migrate to Pt single atoms for participating in the H_2 evolution reaction. The stable and efficient production of H_2 is attributed to the optimal

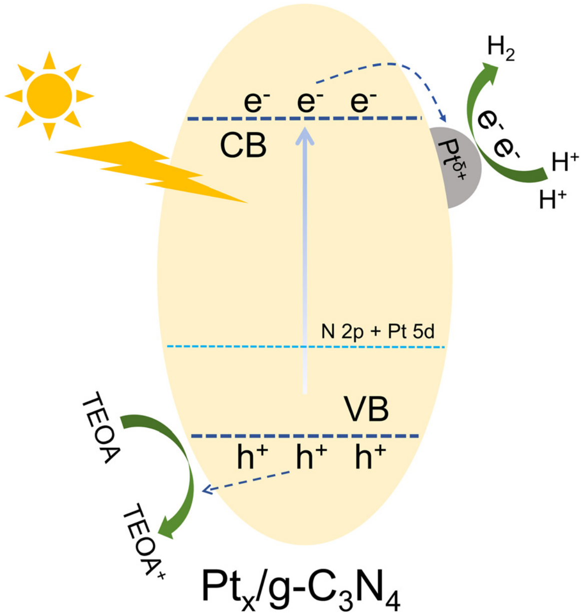

Fig. 11 Mechanism of photocatalytic H_2 production of $Pt_x/g\text{-}C_3N_4$.

dispersion of Pt atoms and the improved charge carrier dynamics facilitated by the interaction between Pt and g-C_3N_4.

4. Conclusions

In summary, Pt_x/g-C_3N_4 photocatalysts with different Pt contents are synthesized using a low-temperature incipient wetness impregnation method. Pt atoms loaded on g-C_3N_4 in the form of the isolated single atoms even at a high density of 1.5 wt% are demonstrated by HAADF–STEM and EXAFS results. The well-dispersed Pt single atoms provide active sites for H^+ adsorption. The Pt single atoms incorporated in the sixfold cavity between the three adjacent triazines form strong interaction between Pt and N_6, which generates new doping energy levels and boosts higher transportation and separation efficiency of photo-generated charge carriers for improving photocatalytic H_2 evolution. The photocatalytic H_2 production rates of Pt_x/g-C_3N_4 are roughly two orders of magnitude better than that of the pristine g-C_3N_4, and the stability increases with increasing Pt loading content. This research reflects a significant advancement in photocatalyst design and opens new avenues for the development of efficient hydrogen production systems.

Author contributions

Qi Zhang: resources, investigation; Miao Yue: investigation, writing – original draft; Peng Chen: investigation, formal analysis; Qingmiao Ren: investigation; Weihu Kong: investigation; Chenxia Jia: visualization, formal analysis; Qianyu Lu: resources, writing – reviewing and editing; Jizhou Wu: formal analysis, writing – original draft; Yuqing Li: methodology; Wenliang Liu: writing – reviewing and editing; Peng Li: visualization; Yongming Fu: conceptualization, investigation, writing – original draft; supervision; and Jie Ma: writing – reviewing and editing, supervision, project administration.

Conflicts of interest

There are no conflicts to declare.

Acknowledgements

This work was supported by the National Key R&D Program of China (2017YFA0304203), the National Natural Science Foundation of China (62020106014, 62175140, 61901249, 92165106, 12104276), PCSIRT (IRT—17R70), 111 project (D18001), the Program for the Outstanding Innovative Teams of Higher Learning Institutions of Shanxi (OIT), the Applied Basic Research Project of Shanxi Province, China (201901D211191, 201901D211188), and the collaborative grant by the Russian Foundation for Basic Research and NSF of China (62011530047, 20-53-53025 in the RFBR classification).

Notes and references

1 C. Bie, L. Wang and J. Yu, Challenges for photocatalytic overall water splitting, *Chem*, 2022, **8**, 1567–1574.

2 T. Hisatomi, J. Kubota and K. Domen, Recent advances in semiconductors for photocatalytic and photoelectrochemical water splitting, *Chem. Soc. Rev.*, 2014, **43**, 7520–7535.

3 B.-J. Ng, L. K. Putri, X. Y. Kong, Y. W. Teh, P. Pasbakhsh and S.-P. Chai, Z-Scheme Photocatalytic Systems for Solar Water Splitting, *Adv. Sci.*, 2020, **7**, 1903171.

4 J. Zhang, G. Ye, C. Zhang, Z. M. Pan, S. B. Wang, G. G. Zhang and X. C. Wang, Heptazine-Based Ordered-Distorted Copolymers with Enhanced Visible-Light Absorption for Photocatalytic Hydrogen Production, *ChemSusChem*, 2022, **15**, e202201616.

5 M. H. Liu, G. G. Zhang, X. C. Liang, Z. M. Pan, D. D. Zheng, S. B. Wang, Z. Y. Yu, Y. D. Hou and X. C. Wang, Rh/Cr_2O_3 and CoO_x Cocatalysts for Efficient Photocatalytic Water Splitting by Poly (Triazine Imide) Crystals, *Angew. Chem., Int. Ed.*, 2023, **62**, e202304694.

6 Q. Wang, G. Zhang, W. Xing, Z. Pan, D. Zheng, S. Wang, Y. Hou and X. Wang, Bottom-up Synthesis of Single-Crystalline Poly (Triazine Imide) Nanosheets for Photocatalytic Overall Water Splitting, *Angew. Chem., Int. Ed.*, 2023, **62**, e202307930.

7 X. Wang, K. Maeda, A. Thomas, K. Takanabe, G. Xin, J. M. Carlsson, K. Domen and M. Antonietti, A metal-free polymeric photocatalyst for hydrogen production from water under visible light, *Nat. Mater.*, 2009, **8**, 76–80.

8 Z. A. Lan, G. G. Zhang and X. C. Wang, A facile synthesis of Br-modified g-C_3N_4 semiconductors for photoredox water splitting, *Appl. Catal., B*, 2016, **192**, 116–125.

9 X. B. Li, J. Xiong, X. M. Gao, J. T. Huang, Z. J. Feng, Z. Chen and Y. F. Zhu, Recent advances in 3D g-C_3N_4 composite photocatalysts for photocatalytic water splitting, degradation of pollutants and CO_2 reduction, *J. Alloys Compd.*, 2019, **802**, 196–209.

10 L. H. Lin, Z. Y. Yu and X. C. Wang, Crystalline Carbon Nitride Semiconductors for Photocatalytic Water Splitting, *Angew. Chem., Int. Ed.*, 2019, **58**, 6164–6175.

11 S. B. Yang, Y. J. Gong, J. S. Zhang, L. Zhan, L. L. Ma, Z. Y. Fang, R. Vajtai, X. C. Wang and P. M. Ajayan, Exfoliated Graphitic Carbon Nitride Nanosheets as Efficient Catalysts for Hydrogen Evolution Under Visible Light, *Adv. Mater.*, 2013, **25**, 2452–2456.

12 Z. P. Yu, Y. F. Li, A. Torres-Pinto, A. P. LaGrow, V. M. Diaconescu, L. Simonelli, M. J. Sampaio, O. Bondarchuk, I. Amorim, A. Araujo, A. M. T. Silva, C. G. Silva, J. L. Faria and L. F. Liu, Single-atom Ir and Ru anchored on graphitic carbon nitride for efficient and stable electrocatalytic/photocatalytic hydrogen evolution, *Appl. Catal., B*, 2022, **310**, 121318.

13 C. J. Wang, J. Xie, N. Chen, W. F. Chen, P. H. Bai and H. Wang, Non-Noble-Metal Catalyst of Cu/g-C_3N_4 for Efficient Photocatalytic Hydrogen Evolution, *ACS Appl. Energy Mater.*, 2021, **4**, 13796–13802.

14 W. Li, X. S. Chu, F. Wang, Y. Y. Dang, X. Y. Liu, X. C. Wang and C. Y. Wang, Enhanced cocatalyst-support interaction and promoted electron transfer of 3D porous g-C_3N_4/GO-M (Au, Pd, Pt) composite catalysts for hydrogen evolution, *Appl. Catal., B*, 2021, **288**, 120034.

15 Z. Wang, Y. Luo, T. Hisatomi, J. J. M. Vequizo, S. Suzuki, S. S. Chen, M. Nakabayashi, L. H. Lin, Z. H. Pan, N. Kariya, A. Yamakata, N. Shibata, T. Takata, K. Teshima and K. Domen, Sequential cocatalyst decoration on $BaTaO_2N$ towards highly-active Z-scheme water splitting, *Nat. Commun.*, 2021, **12**, 1005.

16 C. M. Wolff, P. D. Frischmann, M. Schulze, B. J. Bohn, R. Wein, P. Livadas, M. T. Carlson, F. Jäckel, J. Feldmann, F. Würthner and J. K. Stolarczyk, All-in-one visible-light-driven water splitting by combining nanoparticulate and molecular co-catalysts on CdS nanorods, *Nat. Energy*, 2018, **3**, 862–869.

17 J. D. Xiao, Q. C. Shang, Y. J. Xiong, Q. Zhang, Y. Luo, S. H. Yu and H. L. Jiang, Boosting Photocatalytic Hydrogen Production of a Metal-Organic Framework Decorated with Platinum Nanoparticles: The Platinum Location Matters, *Angew. Chem., Int. Ed.*, 2016, **55**, 9389–9393.

18 Y. Attia and M. Samer, Metal clusters: New era of hydrogen production, *Renew. Sustainable Energy Rev.*, 2017, **79**, 878–892.

19 Y. Chen, L. Soler, C. Cazorla, J. Oliveras, N. G. Bastus, V. F. Puntes and J. Llorca, Facet-engineered TiO_2 drives photocatalytic activity and stability of supported noble metal clusters during H_2 evolution, *Nat. Commun.*, 2023, **14**, 6165.

20 H. Zhai, Z. Liu, J. Tong, Y. Zhang, B. Zhou, P. Tan, R. Sa and J. Pan, Tuning charge transfer between size-controlled Pt cluster and N vacancy engineered ultrathin g-C_3N_4 for efficient photocatalytic hydrogen evolution, *Ceram. Int.*, 2023, **49**, 36857–36865.

21 F.-G. Zhang, M. Cheng, Y.-J. Yuan, Q.-Y. Liu, Q. Cheng and J. Guan, Boosted charge transfer in Pt cluster anchored TiO_2 microspheres with rich oxygen vacancies for solar driven H_2 production from lignocellulosic biomass, *Inorg. Chem. Front.*, 2023, **10**, 7369–7380.

22 X. Z. Fang, Q. C. Shang, Y. Wang, L. Jiao, T. Yao, Y. F. Li, Q. Zhang, Y. Luo and H. L. Jiang, Single Pt Atoms Confined into a Metal-Organic Framework for Efficient Photocatalysis, *Adv. Mater.*, 2018, **30**, 1705112.

23 B. T. Qiao, A. Q. Wang, X. F. Yang, L. F. Allard, Z. Jiang, Y. T. Cui, J. Y. Liu, J. Li and T. Zhang, Single-atom catalysis of CO oxidation using Pt_1/FeO_x, *Nat. Chem.*, 2011, **3**, 634–641.

24 A. Q. Wang, J. Li and T. Zhang, Heterogeneous single-atom catalysis, *Nat. Rev. Chem.*, 2018, **2**, 65–81.

25 Q. Zuo, T. T. Liu, C. S. Chen, Y. Ji, X. Q. Gong, Y. Y. Mai and Y. F. Zhou, Ultrathin Metal-Organic Framework Nanosheets with Ultrahigh Loading of Single Pt Atoms for Efficient Visible-Light-Driven Photocatalytic H_2 Evolution, *Angew. Chem., Int. Ed.*, 2019, **58**, 10198–10203.

26 G. F. S. R. Rocha, M. A. R. da Silva, A. Rogolino, G. A. A. Diab, L. F. G. Noleto, M. Antonietti and I. F. Teixeira, Carbon nitride based materials: more than just a support for single-atom catalysis, *Chem. Soc. Rev.*, 2023, **52**, 4878–4932.

27 Z. Zeng, Y. Su, X. Quan, W. Choi, G. Zhang, N. Liu, B. Kim, S. Chen, H. Yu and S. Zhang, Single-atom platinum confined by the interlayer nanospace of carbon nitride for efficient photocatalytic hydrogen evolution, *Nano Energy*, 2020, **69**, 104409.

28 Y. Xue, Y. Lei, X. Liu, Y. Li, W. Deng, F. Wang and S. Min, Highly active dye-sensitized photocatalytic H_2 evolution catalyzed by a single-atom Pt cocatalyst anchored onto g-C_3N_4 nanosheets under long-wavelength visible light irradiation, *New J. Chem.*, 2018, **42**, 14083–14086.

29 C. Wu, S. Xue, Z. Qin, M. Nazari, G. Yang, S. Yue, T. Tong, H. Ghasemi, F. C. R. Hernandez, S. Xue, D. Zhang, H. Wang, Z. M. Wang, S. Pu and J. Bao, Making g-C_3N_4 ultra-thin nanosheets active for photocatalytic overall water splitting, *Appl. Catal., B*, 2021, **282**, 119557.

30 L. Zhang, R. Long, Y. Zhang, D. Duan, Y. Xiong, Y. Zhang and Y. Bi, Direct Observation of Dynamic Bond Evolution in Single-Atom Pt/C_3N_4 Catalysts, *Angew. Chem., Int. Ed.*, 2020, **59**, 6224–6229.

31 P. Zhou, F. Lv, N. Li, Y. Zhang, Z. Mu, Y. Tang, J. Lai, Y. Chao, M. Luo, F. Lin, J. Zhou, D. Su and S. Guo, Strengthening reactive metal-support interaction to stabilize high-density Pt single atoms on electron-deficient g-C_3N_4 for boosting photocatalytic H_2 production, *Nano Energy*, 2019, **56**, 127–137.

32 L. Wang, R. Tang, A. Kheradmand, Y. Jiang, H. Wang, W. Yang, Z. Chen, X. Zhong, S. P. Ringer, X. Liao, W. Liang and J. Huang, Enhanced solar-driven benzaldehyde oxidation with simultaneous hydrogen production on Pt single-atom catalyst, *Appl. Catal., B*, 2021, **284**, 119759.

33 G. Huang, Q. Niu, J. Zhang, H. Huang, Q. Chen, J. Bi and L. Wu, Platinum single-atoms anchored covalent triazine framework for efficient photoreduction of CO_2 to CH_4, *Chem. Eng. J.*, 2022, **427**, 131018.

34 Y. Hu, Y. Qu, Y. Zhou, Z. Wang, H. Wang, B. Yang, Z. Yu and Y. Wu, Single Pt atom-anchored C_3N_4: A bridging Pt–N bond boosted electron transfer for highly efficient photocatalytic H_2 generation, *Chem. Eng. J.*, 2021, **412**, 128749.

35 D. Vasilchenko, A. Zhurenok, A. Saraev, E. Gerasimov, S. Cherepanova, S. Tkachev, P. Plusnin and E. Kozlova, Highly efficient hydrogen production under visible light over g-C_3N_4-based photocatalysts with low platinum content, *Chem. Eng. J.*, 2022, **445**, 136721.

36 H. Yang, N. Lu, J. Zhang, R. Wang, S. Tian, M. Wang, Z. Wang, K. Tao and F. Ma, S. Peng. Ultra-low single-atom Pt on g-C_3N_4 for electrochemical hydrogen peroxide production, *Carbon Energy*, 2023, **5**, e337.

37 Y. Yao, Z. Huang, P. Xie, L. Wu, L. Ma, T. Li, Z. Pang, M. Jiao, Z. Liang, J. Gao, Y. He, D. J. Kline, M. R. Zachariah, C. Wang, J. Lu, T. Wu, T. Li, C. Wang, R. Shahbazian-Yassar and L. Hu, High temperature shockwave stabilized single atoms, *Nat. Nanotechnol.*, 2019, **14**, 851–857.

38 X. Liu, S. Wang, W. Yu, J. Zhang, S. Fang, J. Zhang, J. Qiu, F. Kong and X. Duan, Single platinum atoms anchored on

holy carbon nitride for efficient photodegradation of sulfonylurea herbicide, *Chem. Eng. J.*, 2022, **446**, 137426.

39 Z. Chen, S. Mitchell, E. Vorobyeva, R. K. Leary, R. Hauert, T. Furnival, Q. M. Ramasse, J. M. Thomas, P. A. Midgley, D. Dontsova, M. Antonietti, S. Pogodin, N. Lopez and J. Perez-Ramirez, Stabilization of Single Metal Atoms on Graphitic Carbon Nitride, *Adv. Funct. Mater.*, 2017, **27**, 1605785.

40 X. Li, W. Bi, L. Zhang, S. Tao, W. Chu, Q. Zhang, Y. Luo, C. Wu and Y. Xie, Single-Atom Pt as Co-Catalyst for Enhanced Photocatalytic H_2 Evolution, *Adv. Mater.*, 2016, **28**, 2427–2431.

41 M. Ou, S. Wan, Q. Zhong, S. Zhang and Y. Wang, Single Pt atoms deposition on g-C_3N_4 nanosheets for photocatalytic H_2 evolution or NO oxidation under visible light, *Int. J. Hydrogen Energy*, 2017, **42**, 27043–27054.

42 X. N. Yang, L. T. Ren, D. C. Jiang, L. S. Yin, Z. J. Li and Y. P. Yuan, Strong Interfacial Chemical Bonding in Regulating Electron Transfer and Stabilizing Catalytic Sites in a Metal-Semiconductor Schottky Junction for Enhanced Photocatalysis, *Small*, 2023, 2308408, DOI: **10.1002/smll.202308408**.

43 J. C. Shen, C. H. Luo, S. S. Qiao, Y. Q. Chen, Y. H. Tang, J. Q. Xu, K. X. Fu, D. W. Yuan, H. F. Tang, H. Zhang and C. B. Liu, Single-Atom Cu Channel and N-Vacancy Engineering Enables Efficient Charge Separation and Transfer between C_3N_4 Interlayers for Boosting Photocatalytic Hydrogen Production, *ACS Catal.*, 2023, **13**, 6280–6288.

44 Y. Zhu, T. Wang, T. Xu, Y. Li and C. Wang, Size effect of Pt co-catalyst on photocatalytic efficiency of g-C_3N_4 for hydrogen evolution, *Appl. Surf. Sci.*, 2019, **464**, 36–42.

45 P. Y. Dong, Y. Wang, A. C. J. Zhang, T. Cheng, X. G. Xi and J. L. Zhang, Platinum Single Atoms Anchored on a Covalent Organic Framework: Boosting Active Sites for Photocatalytic Hydrogen Evolution, *ACS Catal.*, 2021, **11**, 13266–13279.

46 G. G. Zhang, Z. A. Lan, L. H. Lin, S. Lin and X. C. Wang, Overall water splitting by Pt/g-C_3N_4 photocatalysts without using sacrificial agents, *Chem. Sci.*, 2016, **7**, 3062–3066.

47 P. Kuang, Y. Wang, B. Zhu, F. Xia, C.-W. Tung, J. Wu, H. M. Chen and J. Yu, Pt Single Atoms Supported on N-Doped Mesoporous Hollow Carbon Spheres with Enhanced Electrocatalytic H_2-Evolution Activity, *Adv. Mater.*, 2021, **33**, 2008599.

48 X. Wu, H. Zhang, J. Dong, M. Qiu, J. Kong, Y. Zhang, Y. Li, G. Xu, J. Zhang and J. Ye, Surface step decoration of isolated atom as electron pumping: Atomic-level insights into visible-light hydrogen evolution, *Nano Energy*, 2018, **45**, 109–117.

49 Y. J. Cao, D. H. Wang, Y. Lin, W. Liu, L. L. Cao, X. K. Liu, W. Zhang, X. L. Mou, S. Fang and X. Y. Shen, T. Yao. Single Pt Atom with Highly Vacant d-Orbital for Accelerating Photocatalytic H_2 Evolution, *ACS Appl. Energy Mater.*, 2018, **1**, 6082–6088.

50 T. Cui, L. Ma, S. Wang, C. Ye, X. Liang, Z. Zhang, G. Meng, L. Zheng, H.-S. Hu, J. Zhang, H. Duan, D. Wang and Y. Li, Atomically Dispersed Pt-N_3C_1 Sites Enabling Efficient and Selective Electrocatalytic C-C Bond Cleavage in Lignin Models under Ambient Conditions, *J. Am. Chem. Soc.*, 2021, **143**, 9429–9439.

51 N. Cheng, S. Stambula, D. Wang, M. N. Banis, J. Liu, A. Riese, B. Xiao, R. Li, T.-K. Sham, L.-M. Liu, G. A. Botton and X. Sun, Platinum single-atom and cluster catalysis of the hydrogen evolution reaction, *Nat. Commun.*, 2016, **7**, 13638.

52 Z. Xue, M. Yan, X. Wang, Z. Wang, Y. Zhang, Y. Li, W. Xu, Y. Tong, X. Han, C. Xiong, W. Wang, M. Chen, B. Ye, X. Hong, L. Song, H. Zhang, L.-M. Yang and Y. Wu, Tailoring Unsymmetrical-Coordinated Atomic Site in Oxide-Supported Pt Catalysts for Enhanced Surface Activity and Stability, *Small*, 2021, **17**, 2101008.

53 T. He, S. Chen, B. Ni, Y. Gong, Z. Wu, L. Song, L. Gu, W. Hu and X. Wang, Zirconium-Porphyrin-Based Metal-Organic Framework Hollow Nanotubes for Immobilization of Noble-Metal Single Atoms, *Angew. Chem., Int. Ed.*, 2018, **57**, 3493–3498.

54 Q. Liang, Z. Li, X. Yu, Z.-H. Huang, F. Kang and Q.-H. Yang, Macroscopic 3D Porous Graphitic Carbon Nitride Monolith for Enhanced Photocatalytic Hydrogen Evolution, *Adv. Mater.*, 2015, **27**, 4634–4639.

55 X. Li, B. Kang, F. Dong, Z. Zhang, X. Luo, L. Han, J. Huang, Z. Feng, Z. Chen, J. Xu, B. Peng and Z. L. Wang, Enhanced photocatalytic degradation and H_2/H_2O_2 production performance of S-pCN/$WO_{2.72}$ S-scheme heterojunction with appropriate surface oxygen vacancies, *Nano Energy*, 2021, **81**, 105671.

56 E. C. Kohlrausch, H. A. Centurion, R. W. Lodge, X. L. Luo, T. Slater, M. J. L. Santos, S. L. Ling, V. R. Mastelaro, M. J. Cliffe, R. V. Goncalves and J. A. Fernandes, A high-throughput, solvent free method for dispersing metal atoms directly onto supports, *J. Mater. Chem. A*, 2021, **9**, 26676–26679.

57 X. Han, Q. A. Liu, A. Qian, L. Ye, X. Pu, J. C. Liu, X. Jia, R. J. Wang, F. Ju, H. Sun, J. G. Zhao and H. Ling, Transition-Metal Single Atom Anchored on MoS_2 for Enhancing Photocatalytic Hydrogen Production of g-C_3N_4 Photocatalysts, *ACS Appl. Mater. Interfaces*, 2023, **15**, 26670–26681.

58 T. Mahvelati-Shamsabadi, K. C. Bhamu, S. H. Lee, T. T. Dang, V. H. Khoi, S. H. Hur, W. M. Choi, S. G. Kang, T. J. Shin and J. S. Chung, Coordinatively unsaturated atomically dispersed Pt+2-N4 sites on hexagonal nanosheet structure of g-C3N4 for high-performance photocatalytic H2 production, *Appl. Catal., B*, 2023, **337**, 122959.

59 D. W. Sun, C. C. Long and J. H. Huang, Highly dispersed platinum-anchored g-C_3N_4 nanotubes for photocatalytic hydrogen generation, *Int. J. Hydrogen Energy*, 2023, **48**, 943–952.

60 H. Zhai, P. Tan, M. Jiang, M. Zhang, R. Ren, R. Sa and J. Pan, Electronic Regulation of Pt Single-Atom Catalysts via Local Coordination State Adjustment for Enhanced Photocatalytic Performance, *ACS Catal.*, 2023, **13**, 8063–8072.